DOI 10.1007/s11182-020-02014-6

*Russian Physics Journal, Vol. 63, No. 1, May, 2020 (Russian Original No. 1, January, 2020)*

# OPTICS AND SPECTROSCOPY

## PECULIARITIES OF STRUCTURE AND MORPHOLOGY OF COPPER-CERIUM NANOPOWDERS PRODUCED BY LASER ABLATION

**D. A. Goncharova,[1] D. A. Svintsitskiy,[2,3] O. A. Stonkus,[2,3] V. A. Svetlichnyi,[1] and A. I. Boronin[2,3]**

UDC 621.373.826, 621.6.04, 543.428.3

*Copper-cerium nanopowders* $CuO_x$–$CeO_2$ *(mass ratio* Cu:Ce = *6:100) are prepared by mixing the dispersions of the copper and cerium oxides produced by the method of pulse laser ablation (PLA) in liquid, followed by drying. The initial dispersions of copper oxides were prepared by the method of PLA of a metal copper target in distilled water or 1% hydrogen peroxide solution, and those of cerium oxide – by PLA of metal cerium in distilled water. It is shown that ablation of copper in water and water solution of peroxide is followed by the formation of copper oxide particles of different morphologies and compositions (structure). It is established that no crystal phases of copper oxides are formed in the copper-cerium nanopowders produced from separate dispersions. Given this approach to forming copper-cerium nanoparticles, the oxidized copper is distributed in the form of a thin layer on the* $CeO_2$ *surface, which is demonstrated by the results of investigation of these particles by the methods of high-resolution transmission electron microscopy and X-ray diffraction. The formation of a* Cu–O–Ce *interface at the interphase boundary gives rise to the formation of defects on the* $CeO_2$ *surface, which is confirmed by the Raman spectroscopy. An investigation of the composition and electronic structure of the surface of* $CuO_x$ *nanoparticles and* $CuO_x$–$CeO_2$ *nanopowders performed by the method of X-ray photoelectronic spectroscopy reveals the presence of copper in the form of a combination of* Cu (I) *and* Cu (II) *with the prevailing contribution from a single-valence state for* $CuO_x$–$CeO_2$ *nanopowders, which could have resulted from the interaction between* $CuO_x$ *and* $CeO_2$ *particles.*

**Keywords**: copper oxide, copper-cerium nanopowders, pulse laser ablation, nanoparticles, X-ray photoelectronic spectroscopy, Raman spectroscopy.

### INTRODUCTION

Nanoparticles (NPs) of copper and copper-based nanostructures are promising multifunctional materials for different hi-tech applications in optoelectronics [1, 2], sensorics [3, 4], biomedicine [5, 6] and other areas. Among the important practical applications of cupric nanostructures is the surface catalysis [7]. Copper-based catalysts favorably compete with precious metals and are extensively used in the industry for dehydrogenation of alcohols to aldehydes and ketones [8, 9], decomposition of methanol [10], direct decomposition of $N_2O$ to $N_2$ [11], selective catalytic oxidation of ammonia to nitrogen [12], oxidation of CO [13, 14] and other important applied processes. The catalytic properties of

[1]National Research Tomsk State University, Tomsk, Russia, e-mail: dg_va@list.ru; v_svetlichnyi@bk.ru; [2]Boreskov Institute of Catalysis of the Siberian Branch of the Russian Academy of Sciences, Novosibirsk, Russia, e-mail: sad@catalysis.ru; stonkus@catalysis.ru; boronin@catalysis.ru; [3]Novosibirsk National Research State University, Novosibirsk, Russia. Translated from Izvestiya Vysshikh Uchebnykh Zavedenii, Fizika, No. 1, pp. 135–143, January, 2020. Original article submitted October 15, 2019.

 

copper nanostructures strongly depend on the nature and particle size of the active component [9, 15]. Their high catalytic reactivity is frequently dictated by the interaction between the active component and the support [16]. For instance, an extraordinary activity of the copper-cerium catalysts is accounted for by the synergetic oxidation-reduction properties exhibited after the formation of the interface structures between the copper oxide and cerium nanoparticles [16–18]. The ions of the active component can also be embedded into the $CeO_2$ lattice to form the phases of interaction, which also favors the formation of highly dispersed forms of copper [16, 17, 19]. Thus determination of the nature of interaction of highly dispersed $CuO_x$ and $CeO_2$ particles is an important stage in the investigation of highly effective copper-cerium catalysts with the target catalytic properties. Moreover, the knowledge on the evolution of the active component structure on the surface of the support during the reaction treatment is necessary for determination of the catalytic reaction mechanisms. There is an ongoing discussion in the scientific literature related to the CO oxidation mechanism on the copper-cerium catalyst surface. Note that the focus of the discussion is made either on the Langmuir-Hinshelwood or mechanism, or Mars-van Krevelen redox mechanism. This discussion also dictates a necessity of developing new approaches to synthesizing copper-cerium catalysts and the need for their detailed investigation using advanced physical-chemical methods.

By means of the high-energy physical method of pulsed laser ablation (PLA) in liquid [20] nanostructures with unique surface properties can be formed. The uniqueness consists in the absence of the surface stabilizing molecules or strongly adsorbed residual reaction products commonly present during chemical synthesis. The second important feature of the method is a possibility of forming metastable structures in the course of PLA. This is due to the mechanism of NP formation by PLA in liquid. Because of the confinement of the cloud of laser induced plasma by the liquid it rapidly reaches a thermodynamic state characterized by high temperature, pressure and density, which is favorable for the course of chemical reactions inefficient or impossible under ordinary conditions, and the short lifetime of the ablative particles favors the formation of metastable structures [21–23]. The above-mentioned characteristics of the PLA-nanoparticles and their comparative analysis with the NPs formed by the methods of preparative chemistry make the use of the former in catalytic systems quite promising [22, 24].

The purpose of this work is to form $Cu_2O$, CuO and $CuO_x$–$CeO_2$ nanopowders and to perform a comparative analysis of their morphology, structure and surface state. These nanomaterials produced by the PLA method in liquid are promising catalysts of low-temperature CO oxidation.

## FORMATION OF NANOPARTICLES AND METHODS OF ANALYSIS

In order to identify the influence of interaction between highly dispersed $CuO_x$ and $CeO_2$ nanoparticles produced by the PLA method, two types of particles were synthesized and investigated: 1) separate $CuO_x$ and $CeO_2$ nanoparticles and 2) mixed $CuO_x$–$CeO_2$ nanoparticles.

Pulsed laser ablation was performed with a Nd:YAG-laser (LS2131M-20, LOTIS TII) with the wavelength of 1064 nm and pulse energy up to 180 mJ. The pulse duration and repetition frequency were 7 ns and 20 Hz, respectively. The PLA of the targets was performed in a 100 ml glass cup for 60–120 min. Before the ablation, we measured the mass of the target and the volume of the solvent wherein the target was immersed. During PLA, the material removed from the target is transferred into the solution. It mass is determined by the repeated weighting from the difference between the masses. The setup and the procedure of the PLA of copper and cerium are detailed elsewhere [25, 26].

Nanopowders of $CuO_x$ were produced by PLA of copper (99.5% purity) in distilled water and in an aqueous solution of hydrogen peroxide (1wt.%) followed by drying of the dispersions at 60°C. The 1% hydrogen peroxide solution was prepared from the 40% medicine hydrogen peroxide (GOST 177-88) by the method of stepwise dilution.

Copper-cerium nanopowders were synthesized in two stages. For this purpose, firstly the dispersions of individual oxides were formed by the PLA of metal cerium (99.5%) in distilled water and metal copper targets in distilled water or water solution of hydrogen peroxide (1 wt.%). Then the resulting solutions were mixed in the proportions, ensuring a mass ratio of Cu:Ce = 6:100, and then dried on air at the temperature of 60°C. The resulting samples of copper-cerium nanopowders are designated as 6% $Cu_2O/CeO_2$ (PLA of copper in water) and 6% $CuO/CeO_2$ (PLA of copper in a water solution of hydrogen peroxide).

The phase composition of the materials was investigated by the method of X-ray diffraction analysis (XRD) in a Shimadzu XRD 6000 diffractometer (Shimadzu, Japan). The phases were identified with use of PDF-4 database. The unit-cell parameters were calculated using the PowderCell 2.4 software program.

The size, morphology and structure of the particles were investigated in a JEM-2200FS transmission electron microscope (JEOL Ltd., Japan) (accelerating voltage – 200 kV, grid resolution – 1 Å). Dark-field images were obtained in the scanning mode using a HAADF (High-Angle Annular Dark-Field) detector. The microscope is equipped with an EDX power dispersive attachment (JEOL Ltd., Japan) for the local elemental analysis (local resolution up to 1 nm, energy resolution 130 eV). The powders were preliminary dispersed by ultrasound in alcohol and deposited onto nickel meshes coated with amorphous carbon.

The specific surface area of the powders ($S_{sp}$) was determined by the multipoint BET method (Brunauer-Emmet-Teller) from the adsorption of nitrogen in a TriStar II 3020 analyzer (Micromeritics, USA). The samples were degassed in vacuum ($10^{-2}$ Torr) at room temperature for 2 h.

The measurement of photoelectronic spectra was performed in an ES-300 spectrometer (KRATOS Analytical, Great Britain). The primary radiation used in the study was Kα-line of magnesium with the photon energy 1253.6 eV. The X-ray power did not exceed 70 W. The spectrometer was calibrated using the positions $Au4f_{7/2}$ (84.0 eV) and $Cu2p_{3/2}$ (932.7 eV) for pure gold and copper foils, respectively. For the internal spectra calibration, the C1s peak was used with a maximum near 284.8 eV. In the case of cerium – bearing samples, the calibration was carried out using the U′′′ peak in the Ce3d spectra, for which the position of the maximum was taken to be 916.7 eV. The ratio of elements was determined from the respective spectral line areas using the empirical atomic sensitivity factors (ASF) [27].

The Raman spectra (RS) were recorded by an InVia spectrometer (Renishaw, Great Britain) via excitation by the radiation of the 2nd harmonic of a Nd:YAG laser (532 nm) in the range of 100–2500 $cm^{-1}$ with a spectral resolution of 2 $cm^{-1}$.

The spectral properties of powder nanomaterials were investigated by a Cary100 spectrophotometer (Varian, Australia) equipped with a DRA-CA-30I diffuse reflectance accessory (Labsphere, USA). For the experiments the samples were mixed with MgO in the ratio 5:100. The resulting reflection spectra were transformed using the Kubelka–Munch method.

## RESULTS AND DISCUSSION

The morphology, structure and phase composition of $CuO_x$ nanopowders are presented in Fig. 1*a*, *b*. According to the TEM data, the particles formed in water (Fig. 1*a*) have a rectangular shape and a size in the range of 10–50 nm. Typical high-resolution (HR) TEM images demonstrate that the $Cu_2O$ cubic phase is characteristic for the NPs formed in water, which is suggested by a certain combination of interplanar distances – 2.47 and 2.10 Å for the (111) and (200) planes, respectively. Furthermore, the image obtained by the Fourier transform, made for Section I in Fig. 1*a* (corresponding to the [001] zone axis) confirms the presence of the $Cu_2O$ crystal phase. The diffraction patterns from the sample, presented in Fig. 2*a*, also indicate the formation of NPs of a $Cu_2O$ composition.

The NPs formed by the PLA of copper in a water solution of hydrogen peroxide have a different morphology (Fig. 1*b*). They have their individual leaf- or flower-like shapes in the case of aggregations of particles. The combination of interplanar distances of 2.31 and 2.29 Å, corresponding to the (111) and (200) planes of the monoclinic CuO, is consistent with the X-ray diffraction data (Fig. 2*a*). The enlarged region I represents the CuO phase, which is validated by the image with a FFT, corresponding to the [011] zone axis of the CuO crystal. The mechanism of formation of leaf- and flower-like copper oxide structures as a result of PLA of copper in a water solution of hydrogen peroxide is detailed in [28].

In the nanopowders formed via mixing the $CuO_x$ NPs, synthesized by the PLA of copper in water and water solution of hydrogen peroxide, with the $CeO_2$ particles we observe the presence of large polycrystalline particles of spherical shapes about 100 nm in size along with the primary blocks measuring about 10-20 nm and smaller agglomerates (3–5 nm) of particles (Fig. 1*c* and *d*). According to the HR TEM images, both large, well crystallized, and small (2–5 nm) defective particles have the interplanar distances corresponding to the $CeO_2$ phase. According to the EDX data, copper and cerium are uniformly distributed in the samples (Fig. 3). However, near the surface of large

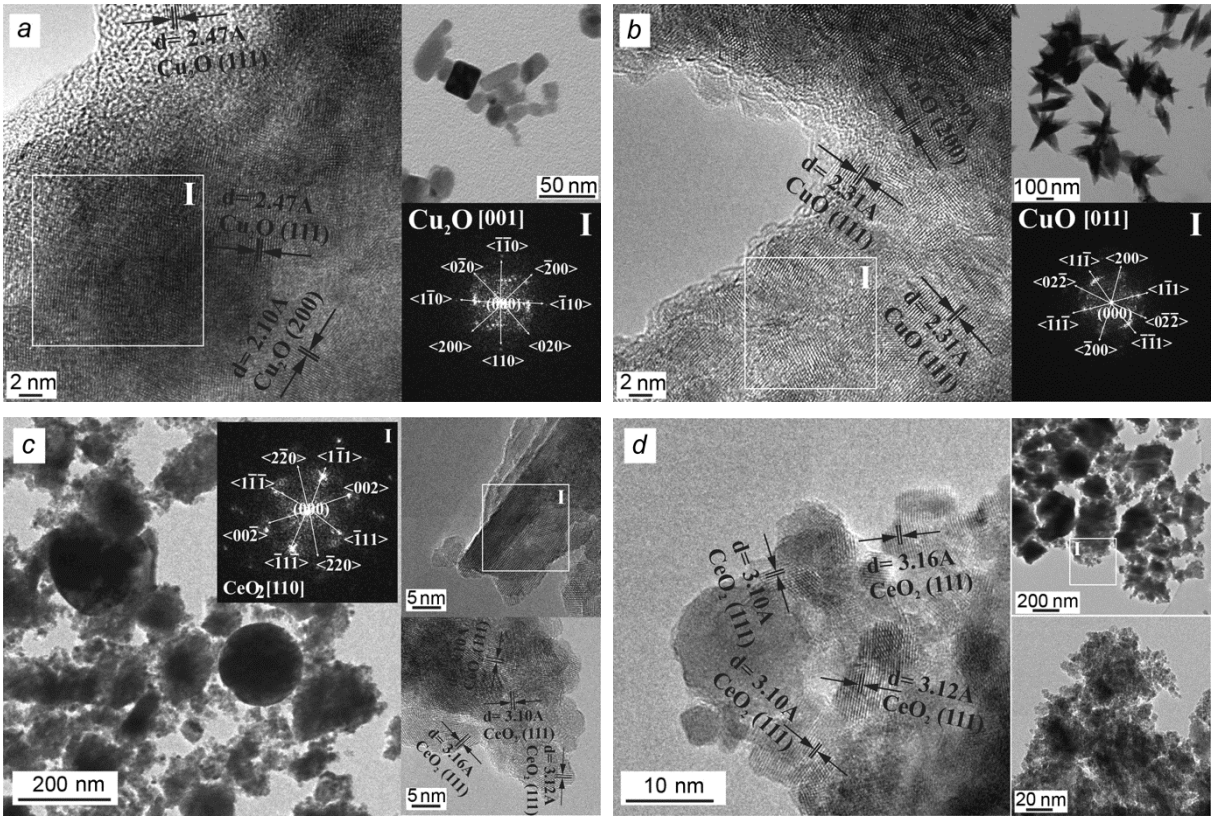


Fig. 1. HR TEM images of NPs formed by the PLA of copper in water (*a*) and water solution of hydrogen peroxide (*b*) of the following compositions: 6% $Cu_2O/CeO_2$ (*c*) and 6% $CuO/CeO_2$ (*d*).

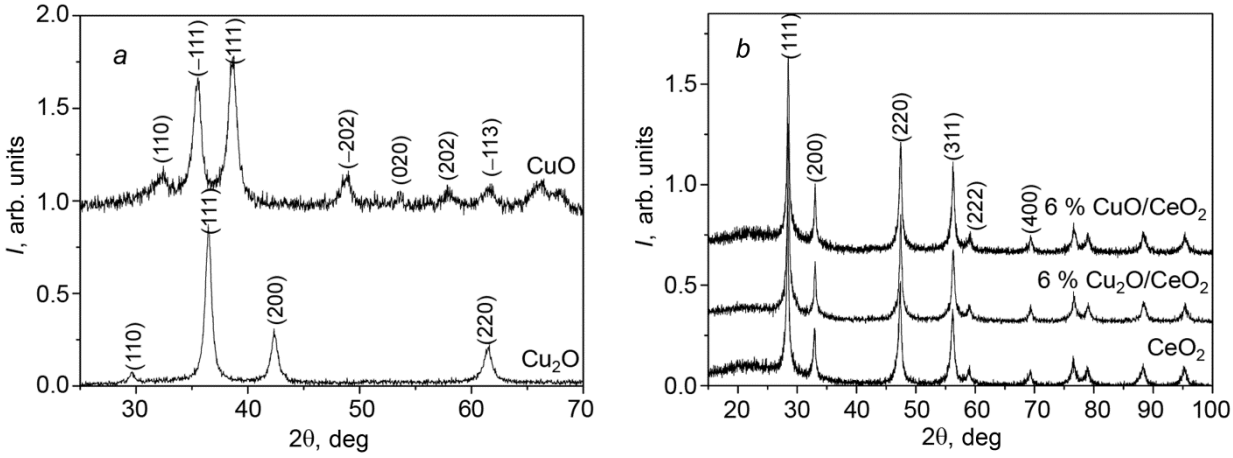


Fig. 2. Diffraction patterns obtained from $CuO_x$ (*a*), $CeO_2$ and mixed $CuO_x$–$CeO_2$ (*b*) nanopowders.

particles the ratio of Cu/Ce signals is observed to increase. According to the calculations performed using the EDX spectra, the copper content in the particle bulk (Region I) is found to be 3.9 at.%, and on surfaces (Region II) it reaches 11.2 at.% (Fig. 3). In the HR TEM images it is impossible to identify the interplanar distances corresponding to individual copper oxides. Note that the morphology of copper-cerium particles is similar to that of pure $CeO_2$ NPs synthesized by the PLA method [29].

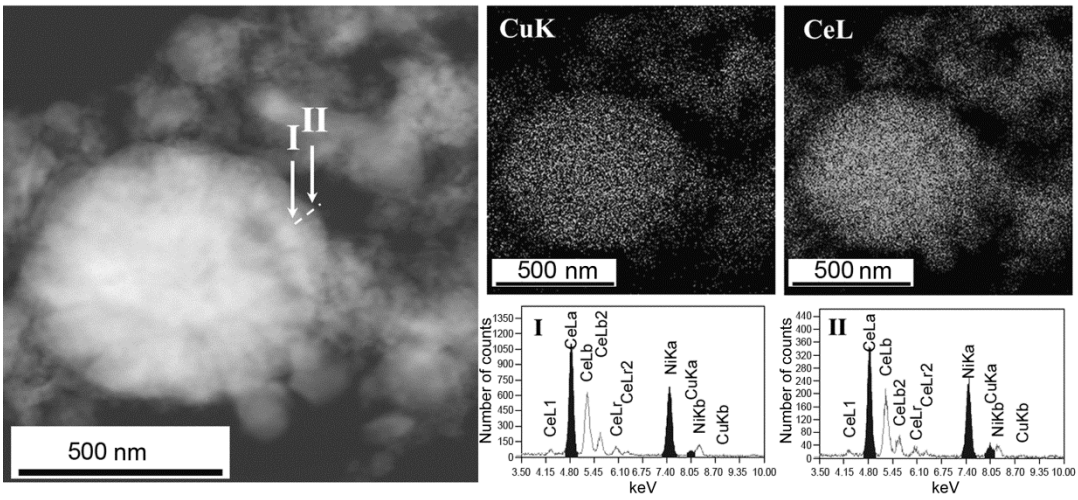


Fig. 3. HAADF-STEM image of an area of the 6% $Cu_2O/CeO_2$ and the corresponding EDX-maps of copper (CuK) and cerium (CeL), the EDX spectra for the enlarged Regions I and II.

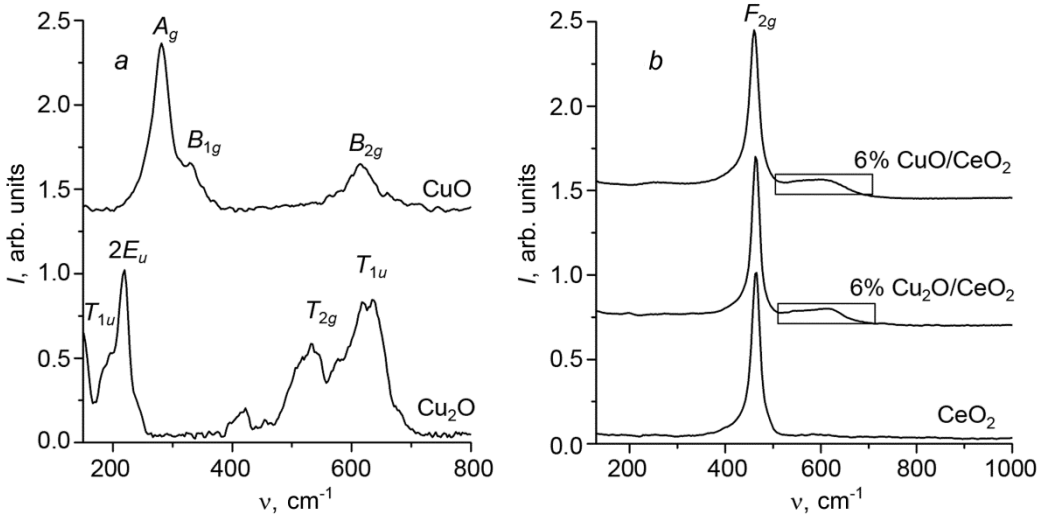


Fig. 4. Raman spectra of the PLA copper oxide (*a*) and copper-cerium samples (*b*).

The diffraction patterns of copper-cerium nanopowders are presented in Fig. 2*b*. The intensive peaks in the diffraction patterns belong to the cerium dioxide phase with the structure of fluorite. There are no reflections corresponding to individual copper oxides in the copper-cerium samples, which correlates with the HR TEM data. Note that for pure well crystallized cerium dioxide, the lattice parameter is $a$ = 5.411 Å [30], and for $CeO_2$ produced by PLA it is $a$ = 5.415 Å. An increase in the fluorite lattice parameter is due to the size refinement of the crystallites [30]. The lattice parameter of copper-cerium nanopowders is slightly higher $a$ = 5.414 Å. A decrease in the lattice parameter of the cerium dioxide for copper-cerium samples can be attributed to partial substitution of Ce ions with Cu ions, since the copper ion radius ($r_{Cu(I)}$ = 77 pm, $r_{Cu(II)}$ = 73 pm) is smaller than that of $Ce^{4+}$ ($r_{Ce(IV)}$ = 92 pm).

The Raman spectra of the nanoparticles and nanopowders are shown in Fig. 4. The spectrum from $Cu_2O$ (Fig. 4*a*) has the following bands: in the region of 150 cm$^{-1}$ belonging to the $T_{1u}$-symmetry, at 220 cm$^{-1}$ – doubly degenerate vibrations of the $E_u$-symmetry, at 350 cm$^{-1}$ – $A_{2u}$-symmetry, at 515 cm$^{-1}$ – a single RS active peak of the $T_{2g}$-

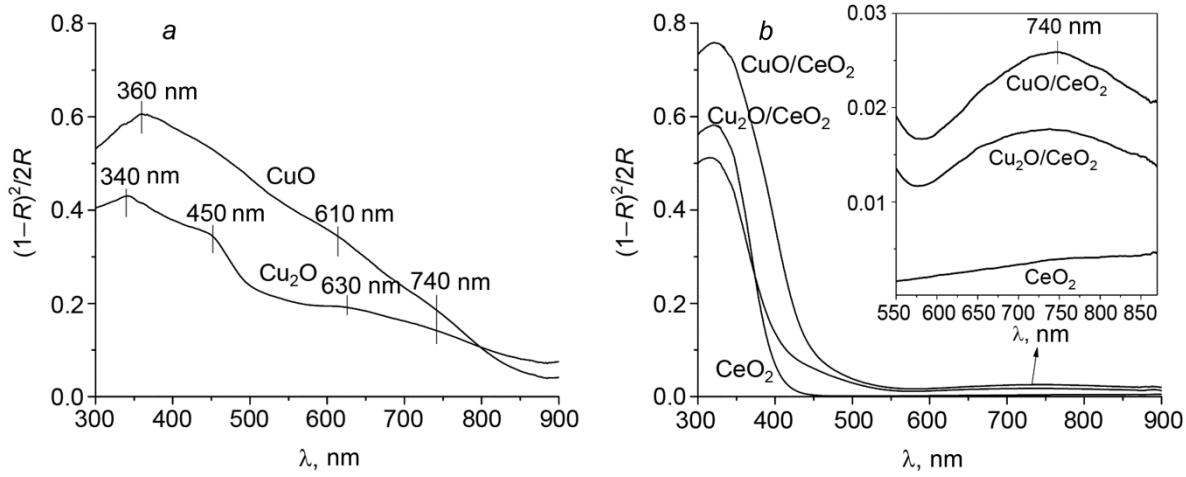


Fig. 5. Absorption spectra in the visible UV-region for the copper oxide nanopowders (*a*) and copper-cerium samples (*b*).

symmetry, in the region of 630–660 $cm^{-1}$ – a band of the $T_{1u}$-symmetry. The peak in the region from 400 to 490 $cm^{-1}$ can be attributed to the multiphoton scattering. An additional signal at 200 $cm^{-1}$ is due to the local fluctuations of atoms of copper [31, 32]. The presence of the vibrational modes not active in the Raman scattering (bands at 150, 200, 220, 350 and 450 $cm^{-1}$) is attributed to the high density of defects in $Cu_2O$ nanoparticles produced by PLA in water [31].

There are only three modes of the $A_g$, $B_{1g}$ and $B_{2g}$ CuO symmetry, which are Raman-active in the region of 290, 340 and 610 $cm^{-1}$ [32] (Fig. 4*a* ) for the PLA-produced samples.

The Raman spectra for the 6% $Cu_2O/CeO_2$ and 6% $CuO/CeO_2$ samples, as well as for pure $CeO_2$ samples are presented in Fig. 4*b*. The peak at 463 $cm^{-1}$, observed for all three samples, corresponds to the vibrational mode $F_{2g}$ typical for the cubic $CeO_2$phase [33, 34]. The broad peak in the region of 520–650 $cm^{-1}$ (region in the box in Fig. 4*b*) corresponds to the vibrations caused by the $CeO_2$ structure defects. According to the literature data, there can be two types of defects in the sample: the anion Frenkel defects, where an oxygen atom is displaced from its position in the lattice towards the interstitial position (peak at 550 $cm^{-1}$) [34]. Note that the formation of oxygen vacancies can indicate partial embedding of copper ions into the $CeO_2$ lattice.

The absorption spectra in the visible UV-region for copper oxide nanopowders are shown in Fig. 5*a*. The $Cu_2O$ powder (Fig. 2*a*) has absorption bands in the region of 340, 450 and 610 nm. The absorption spectrum of the CuO powder, produced by the PLA of copper in hydrogen peroxide, has a band at 360 and weak bends at 610 and 740 nm (Fig. 5*a*). In the general case, it is impossible to identify which of the bands belongs to the copper (I) or (II) oxides, since the peak at 630 nm belongs to the transition in the band gap of CuO, which can appear for the $Cu_2O$ particles due to their oxidation in air [35–37]. The band at 450 nm is attributed to the three-dimensional $Cu^+$ surface clusters in the CuO matrix [38], i.e., this band allows for a simultaneous presence of two forms of oxidized copper – (I) and (II). The absorption in the range 640–740 nm corresponds to the *d*–*d*-transitions in $Cu^{2+}$ of an octahedral configuration with tetragonal distortion [39]. When the degree of lattice distortion increases, this band is displaced towards short wavelengths. The absorption spectra of copper-cerium and pure $CeO_2$ samples are presented in Fig. 2*b*. The absorption in the near UV-region (up to 400 nm) is typical for $CeO_2$ [40]. For the copper-cerium samples the absorption is observed in the long wavelength region (inset in Fig. 5*b*), which is due to the presence of Cu (II) in an octahedral coordination.

The information on the surface composition of the experimental samples determined by the method of X-ray photoelectron spectroscopy (XPS) and BET analysis are presented in Table 1. In order to analyze the state of copper, all possible characteristics (α′-Cu, F-parameter, $Cu2p_{3/2}$) were taken into consideration. F-parameter is calculated as the ratio of the main peak intensity $Cu2p_{3/2}$ to that of the so-called shake-up-satellite in the region of ~941 eV. It is a highly sensitive criterion to identification of the reduced copper forms [41], since the intensive shake-up-satellite is

TABLE 1. XPS and Specific Surface Data for Copper Oxide Powders and Copper-Cerium Nanopowders

| Sample | $Cu2p_{3/2}$, eV | α'-Cu, eV | F-parameter | Cu/Ce | $S_{sp}$, $m^2/g$ |
|---|---|---|---|---|---|
| $Cu_2O$ | 932.6 | 1849.3 | 16.6 | – | 29 |
| CuO | 933.5 | 1850.9 | 2.9 | – | 66 |
| 6% $Cu_2O/CeO_2$ | 933.0 | 1849.6 | 5.8 | 0.165 | 56 |
| 6% $CuO/CeO_2$ | 933.2 | 1850.0 | 5.2 | 0.204 | 43 |

Note. $Cu2p_{3/2}$ – maximum of the strongest copper line, α'-Cu – Auger-parameter, F-parameter – ratio of the $Cu2p_{3/2}$ intensity to the shake-up-satellite intensity (in the region of ~941 eV), Cu/Ce – Cu-to-Ce atomic ratio.

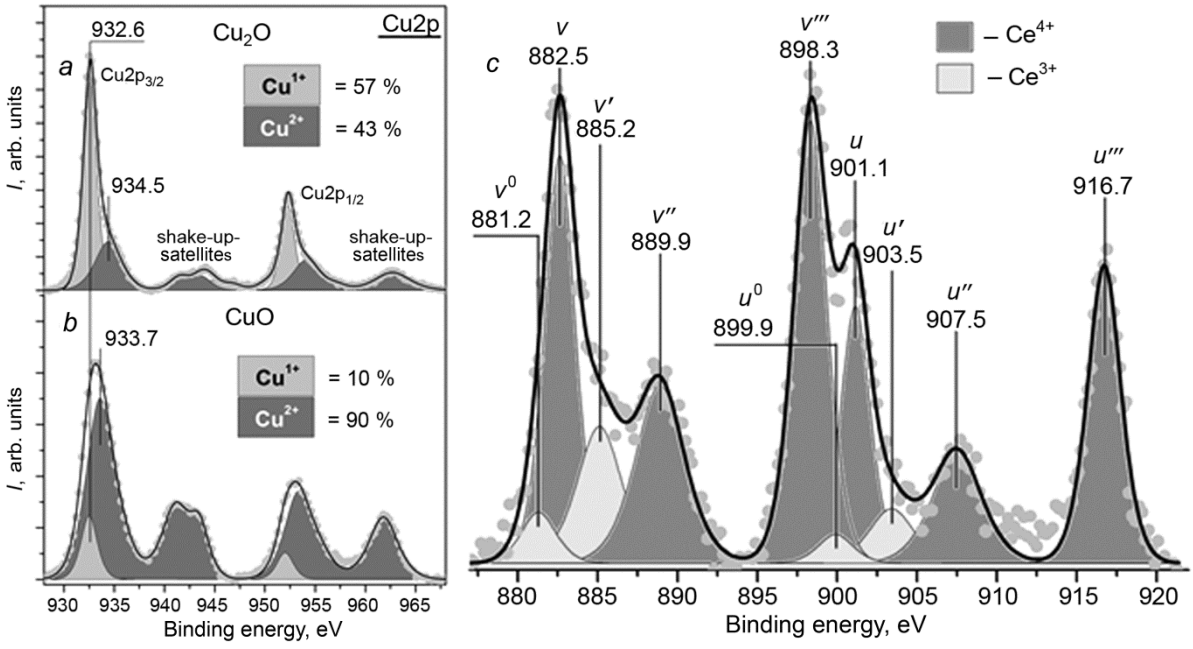


Fig. 6. XPS-spectra broken down into components for the Cu2p band of the $Cu_2O$ (*a*) and CuO (*b*) NPs and for the Ce3d band of the 6% $CuO/CeO_2$ (*c*) sample.

a characteristic attribute of the two-valence copper only [42, 43]. The higher the value of F-parameter, the higher the content of reduced copper. The value of F-parameter for copper oxide (II) particles, whose surface does not have any reduced $Cu^0$ and/or $Cu^{1+}$forms, is commonly found to be 2.4 ± 0.1 [44, 49]. At the same time, the value of F-parameter for pure $Cu_2O$ oxide tends to infinity, as is the case with metal foil, due to the absence of any shake-up-satellites in the region of ~941 eV.

On the surfaces of $Cu_2O$ and CuO powders, copper is found in the form of a combination of divalent ($E_{BE}$ ($Cu2p_{3/2}$) > 933.5 eV) and monovalent ($E_{BE}$ ($Cu2p_{3/2}$) ~ 932.6 eV) states (Fig. 6*a*, *b*). The most oxidized copper particles were formed by the ablation in the hydrogen peroxide solution (content of $Cu^{2+}$ ~ 90%). In the absence of hydrogen peroxide in water the content of di- and monovalent copper on the particle surfaces was close to 43 and 57%, respectively. It should be noted that the position of the $Cu2p_{3/2}$ peak in the range between 934.5–935 eV for the PLA-particles formed in water is more typical for the $Cu(OH)_2$ copper hydroxide [47, 48]. The Auger parameters of (α′-Cu) copper, calculated as the sum of the binding energy of the $Cu2p_{3/2}$ peak and kinetic energy of the Cu $L_3M_{45}M_{45}$ peak for

nanoparticles with the $Cu_2O$ and CuO structures, were close to 1849.3 and 1850.9 eV, respectively, which supports the preferred monovalent and divalent nature of copper on their surfaces [7, 48, 49].

An analysis of the Ce3d spectra of copper-cerium nanopowders allowed determining the cerium charge state on the surface. An example of such a spectrum distribution is presented in Fig. 6*c*. The $Ce^{3+}$ state has two corresponding doublet components ($v^0/u^0$, $v'/u'$), while $Ce^{4+}$ – three doublets ($v/u$, $v''/u''$ and $v'''/u'''$). On the whole, for the experimental samples the ground state was the $Ce^{4+}$ form with a minor amount of the $Ce^{3+}$form. The fraction of the latter was close to (16 ± 4)%, which is typical for the $CeO_2$-based systems [50, 51].

The characteristics demonstrating the content and state of copper on the surfaces of copper-cerium nanopowders are also presented in Table 1. Note that the atomic ratio of copper and cerium (expressed as Cu/Ce) on the surfaces of the 6% $Cu_2O/CeO_2$ and 6% $CuO/CeO_2$ samples was close to approximately 0.165 and 0.204, respectively, which is somewhat lower than the mole ratio of copper and cerium (Cu:Ce = 0.13:1) in the sample composition. This suggests that copper is non-uniformly distributed over the volume of copper-cerium particles: the cerium oxide particle surfaces are enriched in copper.

The 6% $Cu_2O/CeO_2$ and 6% $CuO/CeO_2$ samples demonstrated a large contribution of univalent copper on the surface, which was supported by comparatively high values of their F-parameter equal to 5.8 and 5.2, respectively. It is well known that the $Cu^{1+}$ centers can form as a result of strong interaction of oxidized copper and cerium oxide nanoparticles/clusters, which results in the reduction of $Cu^{2+}$ to $Cu^{1+}$, with embedding of the latter into the fluorite structure or their stabilization at the interface [52, 53].

Note that the accumulated data on the experimental nanopowders obtained by the physical-chemical methods (TEM, XPS, XRD, Raman spectroscopy) demonstrate that the copper-cerium samples, produced by mixing and drying of copper and cerium oxide dispersions, represent the particles with the fluorite structure whose surface is enriched in copper. Furthermore, irrespective of the nature of the oxidized copper particles in the compositions of initial dispersions ($Cu_2O$ or CuO), we observed stabilization of the univalent copper on the surface of copper-cerium particles. This is likely to be due to interaction between $CuO_x$ and $CeO_2$ followed by the formation of a Cu–O–Ce-interface, which results in the oxidized copper distribution over the $CeO_2$ particle surfaces in the form of a thin X-ray amorphous layer. If that is the case, the high dispersiveness of the oxidized copper on the $CeO_2$ surface accounts for the increased contribution from the divalent copper (F-parameter ~ 5.8, Table 1) compared to individual particles of $Cu_2O$, produced by PLA in water (F-parameter ~ 16.6, Table 1).

## SUMMARY

The investigations have shown that nanoparticles of different shapes and compositions are formed in the course of PLA of a copper target in water and water solution of hydrogen peroxide. While cubic $Cu_2O$ NPs are formed in water, leaf- and flower-like CuO particles – in a water solution of hydrogen peroxide. In the case of formation of copper-cerium nanopowders by mixing and drying of the copper and cerium oxide dispersions, the $CuO_x$ structures are stabilized on the $CeO_2$ surface, which is consistent with the XRD and TEM data. Furthermore, the formation of a Cu–O–Ce interface is very likely at the interphase boundary in these samples, which favors pinning of the defects on the $CeO_2$ surface, according to the Raman spectroscopy data. An investigation by the method of photoelectron spectroscopy has demonstrated that in all of the experimental samples copper is present in the form of a combination of its Cu (I) and Cu (II) states. Irrespective of the method of formation of the $CuO_x$–$CeO_2$ copper-cerium samples, a large fraction of univalent copper is stabilized on their surfaces, which could be due to interaction between the $CuO_x$ and $CeO_2$ particles.

Both the copper oxide nanopowders and copper-cerium samples produced by the PLA method will be further investigated as the catalysts in the low-temperature CO oxidation reaction.

This study has been performed with a financial support of the RFBR within a scientific project No. 19-33-50028_mol_nr.

**REFERENCES**


1. J. Neddersen, G. Chumanov, and T. M. Cotton, Appl. Spectrosc., **47**, 1959–1964 (1993).
2. A.P. Wanninayake, S. Gunashekar, S. Li, *et al*., Semicond. Sci. Technol., **30** (064004), 1–7 (2015).
3. K. Mikami, Y. Kido, Y. Akaishi, *et al*., Sensors, **19** (211), 1–14 (2019).
4. A. V. Shabalina, V. A. Svetlichnyi, K. A. Ryzhinskaya, *et al*., Anal. Sci., **33** (12), 1415–1419 (2017).
5. A. D. Badaraev, A. L. Nemoykina, E. N. Bolbasov, *et al*., Resource-Efficient Technol**3** (2), 204–211 (2017).
6. V. A. Svetlichnyi, D. A. Goncharova, A. V. Shabalina, *et al*., Nano Hybr. Compos., **13**, 75–81 (2017).
7. D. A. Svintsitskiy, T. Y. Kardash, O. A. Stonkus, *et al*., J. Phys. Chem. C, **117**, 14588−14599 (2013).
8. A. Gil, P. Ruiz, and B. Delmon, J. Catal., **159** (2), 496–499 (1996).
9. J. Cunningham, G. H. Al-Sayyed, J. A. Cronin, *et al*., J. Catal., – 1986. – V. **102** (1), 160–171 (1986).
10. D. F. Cox and K. H. Schulz, J. Vac. Sci. Technol. A, **8** (3), 2599–2604 (1990).
11. N. Pasha, N. Lingaiah, P. Siva Sankar Reddy, *et al*., Catal. Lett., **127** (1),101–106 (2009).
12. M. Jabłońska, M. Nocuń, K. Gołąbek, *et al*., Appl. Surf. Sci., **423**, 498–508 (2017).
13. J. Laine, J. Brito, F. Severino, *et al*., Catal. Lett., **5** (1), 45–54 (1990).
14. A. J. Elliott, R. A. Hadden, J. Tabatabaei, *et al*., J. Catal., **157** (1), 153–161 (1995).
15. A. Martinez-Arias, D. Gamarra, M. Fernandez-Garcia, *et al*., Catal. Today, **143** (3), 211–217 (2009).
16. W.-W. Wang, W.-Z. Yu, P.-P. Du, *et al*., ACS Catal., **7** (2), 1313–1329 (2017).
17. W. Shan, Z. Feng, Z. Li, *et al*., J. Catal., **228** (1), 206–217 (2004).
18. D. Gamarra, G. Munuera, A. B. Hungría, *et al*., J. Phys. Chem. C, **111** (29), 11026–11038 (2007).
19. S. T. Hossain, E. Azeeva, K. Zhang, *et al*., Appl. Surf. Sci., **455**, 132–143 (2018).
20. H. Zeng, X.-W. Du, S. C. Singh, *et al*., Adv. Funct. Mater., **22**, 1333–1353 (2012).
21. D. Zhang, B. Gökce, and S. Barcikowski, Chem. Rev., **117** (5), 3990–4103 (2017).
22. S. Reichenberger, G. Marzun, M. Muhler, *et al*., Chem. Cat. Chem., **11** (18), 4489–4518 (2019).
23. A. Nath, P. Sharma, and A. Khare, Laser Phys. Lett., **15** (026001), 1–9 (2018).
24. D. Zhang, J. Liu, P. Li, *et al*., Chem. Nano Mat., **3**, 512–533 (2017).
25. V. A. Svetlichnyi and I. N. Lapin, Russ. Phys. J., **58**, No. 11, 1598–1604 (2015).
26. D. A. Goncharova, I. N. Lapin, E. S. Saveliev, *et al*., Russ. Phys. J., **60**, No. 7, 1197–1205 (2017).
27. NIST X-ray Photoelectron Spectroscopy Database, version 4.1; National Institute of Standards and Technology: Gaithersburg, MD, 2012; http://srdata.nist.gov/xps/.
28. D. A. Goncharova, T. S. Kharlamova, V. A. Svetlichnyi, *et al*., J. Phys. Chem. C, **123** (35), 21731–21742 (2019).
29. E. M. Slavinskaya, T.Yu. Kardash, R. V. Gulyaev, *et al*., Catal. Sci. Technol., **6** (17), 6650–6666 (2016).
30. W. Shan, Z. Feng, Z. Li, *et al*., J. Catal., **228** (1), 206–217 (2004).
31. B. K. Meyer, A. Polity, D. Reppin, *et al*., Phys. Status Solidi B, **249** (8), 1487–1509 (2012).
32. L. Debbichi, M. C. Marco de Lucas, J. F. Pierson, *et al*., J. Phys. Chem. C, **116**, 10232–10237 (2012).
33. S. Sun, D. Mao, J. Yu, *et al*., Catal. Sci. Technol., **5** (6), 3166–3181 (2015).
34. S. Agarwal, X. Zhu, E. J. M. Hensen, *et al*., J. Phys. Chem. C, **118** (8), 4131– 4142 (2014).
35. D. B. Pedersen, S. Wang, and S. H. Liang, J. Phys. Chem. C, **112** (24), 8819–8826 (2008).
36. M. Yin, C.-K. Wu, Y. Lou, *et al*., J. Am. Chem. Soc., **127** (26), 9506–9511 (2005).
37. K. Borgohain, N. Murase, and S. Mahamuni, J. Appl. Phys., **92** (3), 1292–1297 (2002).
38. P. W. Baumeister, Phys. Rev., **121,** 359–362 (1961).
39. S. De Tavernier and R. A. Schoonheydt, Zeolites, **11** (2), 155–163 (1991).
40. A. Bensalem, J. C. Muller, and F. Bozon-Verduraz, J. Chem. Soc. Faraday Trans., **88** (1), 153–154 (1992).
41. D. A. Svintsitskiy, A. P. Chupakhin, E. M. Slavinskaya, *et al*., J. Mol. Catal. A Chem., **368**–**369**, 95–106 (2013).
42. N. Pauly, S. Tougaard, and F. Yubero, Surf. Sci., **620**, 17–22 (2014).
43. D. A. Svintsitskiy, A. I. Stadnichenko, D. V. Demidov, *et al*., Appl. Surf. Sci., **257**, 8542–8549 (2011).
44. D. A. Svintsitskiy, T. Y. Kardash, E. M. Slavinskaya, *et al*., Appl. Surf. Sci., **427**, 363–374 (2018).
45. C. D. Wagner, A. V. Naumkin, A. Kraut-Vass, *et al*., Natl. Inst. Stand. Technol., Gaithersburg (2003).

46. J. F. Moulder, W. F. Stickle, P. E. Sobol, *et al*., Perkin-Elmer Corp, Eden Prairie, Minnesota, USA (1992).
47. D. A. Svintsitskiy, L. S. Kibis, A. I. Stadnichenko, *et al*., Kinet. Catal., **54**, 497–504 (2013).
48. G. Schon, Surf. Sci., **35**, 96–108 (1973).
49. D. A. Svintsitskiy, E. M. Slavinskaya, T. Y. Kardash, *et al*., Appl. Catal. A. Gen., **510**, 64–73 (2016).
50. L. S. Kibis, D. A. Svintsitskiy, T. Y. Kardash, *et al*., Appl. Catal. A. Gen., **570**, 51–61 (2019).
51. M. M. Zyryanova, P. V. Snytnikov, R. V. Gulyaev, *et al*., Chem. Eng. J., **238**, 189–197 (2014).
52. Y. Liu, Q. Fu, and M. F. Stephanopoulos, Catal. Today, **93**–**95**, 241–246 (2004).
53. W. Liu and M. F. Stephanopoulos, Chem. Eng. J. Biochem. Eng. J., **64**, 283–294 (1996).